

## Research article

# Fabrication of $Mn_{1-x}Zn_xFe_2O_4$ ferrofluids from natural sand for magnetic sensors and radar absorbing materials



Ahmad Taufiq <sup>a,\*</sup>, Syamsul Bahtiar <sup>b</sup>, Rosy Eko Saputro <sup>a</sup>, Defi Yuliantika <sup>a</sup>, Arif Hidayat <sup>a</sup>, Sunaryono Sunaryono <sup>a</sup>, Nurul Hidayat <sup>a</sup>, Samian Samian <sup>c</sup>, Siriwat Soontaranon <sup>d</sup>

<sup>a</sup> Department of Physics, Faculty of Mathematics and Natural Sciences, Universitas Negeri Malang, Jl. Semarang No 5, Malang 65145, Indonesia

<sup>b</sup> Department of Metallurgy, Faculty of Engineering, Universitas Teknologi Sumbawa, Jl. Raya Olat Maras, Sumbawa, 84371, Indonesia

<sup>c</sup> Department of Physics, Faculty of Science and Technology, Universitas Airlangga, 60115 Surabaya, Indonesia

<sup>d</sup> Synchrotron Light Research Institute, 111 University Avenue, Nakhon Ratchasima 30000, Thailand

## ARTICLE INFO

## Keywords:

Materials science  
Nanotechnology  
Electromagnetism  
Natural sand  
 $Mn_{1-x}Zn_xFe_2O_4$   
Ferrofluid  
Magnetic sensor  
Radar absorbing material

## ABSTRACT

$Mn_{1-x}Zn_xFe_2O_4$  ferrofluids were produced from natural sand for magnetic sensors and radar absorbing materials. The X-ray diffraction data showed that the Zn partially substituted the Mn and Fe ions to construct a spinel structure. The increasing Zn composition decreased the lattice parameters of the structure. The transmission electron microscopy images showed that the filler  $Mn_{1-x}Zn_xFe_2O_4$  nanoparticles tended to agglomerate in three dimensions. Lognormal and mass fractal models were used to fit the small-angle X-ray scattering data of the ferrofluids demonstrated that the ferrofluids formed chain-like structures with a fractal dimension of 1.12–1.67 that was constructed from primary particles with sizes of 3.6–4.1 nm. The filler, surfactant, and carrier liquid of the ferrofluids were confirmed by the functional groups of the metal oxides, tetramethylammonium hydroxide, and  $H_2O$ , respectively. The secondary particles contributed to the saturation magnetization of the  $Mn_{1-x}Zn_xFe_2O_4$  ferrofluids. The  $Mn_{1-x}Zn_xFe_2O_4$  ferrofluids demonstrated excellent performance as magnetic sensors with high stability, especially compared with  $MnFe_2O_4$  ferrofluids. Furthermore, the ferrofluids exhibited excellent radar absorbing materials. The  $Mn_{1-x}Zn_xFe_2O_4$  ferrofluids prepared in this work may serve as a future platform for advancing magnetic sensors and radar absorbing materials.

## 1. Introduction

In the last few years, fabrication methods for producing spinel  $MnZn$  ferrite ( $Mn_{1-x}Zn_xFe_2O_4$ ) nanoparticles with high quality structural and magnetic properties have been developed [1]. The development has also intended to improve the specific application performance of  $Mn_{1-x}Zn_xFe_2O_4$  nanoparticles, especially for sensors [2] and radar or microwave absorbing materials [3]. In general, the application of  $Mn_{1-x}Zn_xFe_2O_4$  nanoparticles has been triggered by their fascinating characteristics, such as excellent magnetic loss, good corrosion resistance, moderate saturation magnetization, and low cost [4]. The  $Mn_{1-x}Zn_xFe_2O_4$  nanoparticles have also been proposed for practical applications, including sensors, owing to their high magnetization sensitivity to temperature [5]. Furthermore, the  $Mn_{1-x}Zn_xFe_2O_4$  nanoparticles have high reflection loss and broadband absorption, providing a significant advantage as a radar absorbing material [6, 7]. However, until recently, there were at least two main challenges with producing

$Mn_{1-x}Zn_xFe_2O_4$  nanoparticles for magnetic sensors and radar absorbing materials with excellent performance. The first issue is producing  $Mn_{1-x}Zn_xFe_2O_4$  nanoparticles with a specific hierarchical structure, such as chain-like structure, with high stability and sensitivity under a small external magnetic field. The second issue is producing  $Mn_{1-x}Zn_xFe_2O_4$  nanoparticles in mass production using simple, inexpensive, effective, and ecofriendly synthesis.

To overcome the first issue, it is essential to produce small  $Mn_{1-x}Zn_xFe_2O_4$  magnetic nanoparticles in a monodisperse system by using a suitable surfactant agent to prevent agglomeration. In this study, we employed a single surfactant technique to coat magnetic particles with tetramethylammonium hydroxide (TMAH). The use of a surfactant is crucial to produce monodisperse magnetic nanoparticles with superparamagnetic characteristics [8, 9]. Fabricating magnetic nanoparticles in a ferrofluid system is an ideal experiment to address the structure issue. Practically, ferrofluids have specific advantages compared with bulk, film, and even in nanopowder forms. One such benefit is that

\* Corresponding author.

E-mail address: [ahmad.taufiq.fmipa@um.ac.id](mailto:ahmad.taufiq.fmipa@um.ac.id) (A. Taufiq).

ferrofluids can maintain magnetic properties in their liquid form and are very sensitive to external magnetic fields [10, 11], which is required for magnetic sensor applications. Interestingly, the interaction between magnetic nanoparticles and external magnetic fields is contributed to by the magnetic moment and liquid flexibility, making magnetic particles in ferrofluids easier to align under an external magnetic field [12]. In addition, ferrofluids can also maintain the properties of a fluid even in the presence of high magnetic fields, and magnetic particles as fillers do not separate from the carrier fluid to provide additional advantages for sensors and radar absorber applications.

To address the second issue, we proposed a fabrication method that uses an abundant natural material as the primary precursor to produce  $Mn_{1-x}Zn_xFe_2O_4$  ferrofluids. To the best our knowledge, the fabrication of  $Mn_{1-x}Zn_xFe_2O_4$  nanoparticles for ferrofluids tends to use relatively expensive commercial primary precursors that are less economical for mass production [5, 13, 14]. Therefore, in this study, we developed a fabrication method of  $Mn_{1-x}Zn_xFe_2O_4$  ferrofluids using abundant natural iron sand as the main precursor that is effective, efficient, inexpensive, and ecofriendly. Natural iron sand can be employed effectively to minimize the fabrication cost for the synthesis of high quality magnetic nanoparticles [15]. Moreover, to further reduce the fabrication cost, water was used as the polar carrier liquid in the fabrication of  $Mn_{1-x}Zn_xFe_2O_4$  ferrofluids with a chain-like structure. The prepared ferrofluids were investigated by their hierarchical nanostructures, molecular structures, and magnetic properties. Finally, the performance of the  $Mn_{1-x}Zn_xFe_2O_4$  ferrofluids as magnetic sensors and radar absorbing materials were also explored.

## 2. Experimental methods

In this study, natural iron sand was used as the primary source of Fe by the formation of ferric chloride and ferrous chloride.  $MnCl_2 \cdot H_2O$  was used as the primary source of Mn and  $ZnCl_2$  was employed as the main source of Zn. The other materials were TMAH used as the surfactant,  $H_2O$  used as the carrier liquid, HCl (38%) used as the solvent, and  $NH_4OH$  (25%) used as the precipitating agent. Dried natural iron sand was separated from impurities using a permanent magnet to produce  $Fe_3O_4$  powder with a purity of 99.5% [15]. Twenty grams of  $Fe_3O_4$  powder was reacted with 58 mL of HCl using a magnetic stirrer for 30 min at room temperature to obtain ferric chloride and ferrous chloride. The ferric chloride and ferrous chloride were reacted with  $MnCl_2 \cdot H_2O$  and  $ZnCl_2$  at specific compositions under stirring for 30 min, followed by a sonication process in a room temperature ultrasonic bath at a frequency of 40 kHz for 10 min. The next process was titration with 27 mL of  $NH_4OH$  for 30 min to obtain a black precipitate consisting of  $Mn_{1-x}Zn_xFe_2O_4$  nanoparticles. The precipitate was then filtered and washed using distilled water until the pH was 7. The  $x$  value of  $Mn_{1-x}Zn_xFe_2O_4$  representing Zn and Mn ions was varied, resulting in compositions of  $Fe_3O_4$ ,  $MnFe_2O_4$ ,  $Mn_{0.75}Zn_{0.25}Fe_2O_4$ ,  $Mn_{0.5}Zn_{0.5}Fe_2O_4$ ,  $Mn_{0.25}Zn_{0.75}Fe_2O_4$ , and  $ZnFe_2O_4$ . Subsequently, 1.2 g of  $Mn_{1-x}Zn_xFe_2O_4$  nanoparticles were reacted with 1.2 mL of TMAH under rough stirring for 15 min to obtain a homogeneous suspension. Five milliliters of  $H_2O$  was then added to the suspension as a dispersant media and stirred for 15 min to obtain the  $Mn_{1-x}Zn_xFe_2O_4$  ferrofluids.

X-ray diffractometry (XRD; X'Pert Pro, PANalytical) was used to determine the phase, particle size, and lattice parameters of the samples. The morphology of the samples was identified using transmission electron microscopy (TEM; JEOL 1400). Characterization of the functional group of the  $Mn_{1-x}Zn_xFe_2O_4$  ferrofluids was performed using Fourier-transform infrared spectroscopy (FTIR; Shimadzu). The magnetic properties were identified using vibrating magnetometer samples (VSM; Oxford). The hierarchical nanostructure of the  $Mn_{1-x}Zn_xFe_2O_4$  ferrofluids was investigated using a synchrotron-based small-angle X-ray scattering (SAXS). Finally, the potential application of the samples was examined by characterization of the magnetic sensor performance in a magnetic field range of 0–200 mT. The relaxation particle time was also investigated at

room temperature. The radar absorption performance of the samples was evaluated using a vector network analyzer (VNA) at a frequency range of 8–12 GHz, which was the working area of the radar.

## 3. Results and discussion

The X-ray diffraction patterns of the  $Mn_{1-x}Zn_xFe_2O_4$  nanoparticles as fillers are depicted in Figure 1. The green lines represent the fitting model using AMCSd No. 0007423 and the experimental data are represented by the black circles. The Rietveld refinement method was employed using the Rietica program to investigate the crystal structure and particle size of the  $Mn_{1-x}Zn_xFe_2O_4$  nanoparticles [16]. Visually, the most intense diffraction peak was Miller index (311), which tended to shift to a lower  $2\theta$  value originating from the Zn ion composition. Quantitatively, the highest diffraction peak of the  $Fe_3O_4$  nanoparticles was detected at  $35.66^\circ$   $2\theta$ , while the highest diffraction peak of the  $MnFe_2O_4$  nanoparticles shifted to a lower  $2\theta$  value at  $35.48^\circ$ . The shifting of the highest diffraction peak originated with the presence of Mn substitution into the  $Fe_3O_4$  nanoparticles [17, 18] owing to the difference in  $Fe^{2+}$ ,  $Fe^{3+}$ , and  $Mn^{2+}$  ionic radii of 0.77, 0.65, and 0.82 Å, respectively [19, 20]. Therefore, the lattice parameters increased, leading to a shift in the diffraction peak to a lower position. Furthermore, the higher Zn ion composition in the  $Mn_{0.75}Zn_{0.25}Fe_2O_4$ ,  $Mn_{0.5}Zn_{0.5}Fe_2O_4$ ,  $Mn_{0.25}Zn_{0.75}Fe_2O_4$ , and  $ZnFe_2O_4$  samples tended to increase the highest diffraction peak position to  $35.59^\circ$ ,  $35.62^\circ$ ,  $35.64^\circ$ , and  $35.71^\circ$ , respectively. The increasing  $2\theta$  values with decreasing lattice parameters originated from the increasing Zn ions with an ionic radii of 0.74 Å, which is smaller than that of the Mn ions [21]. The lattice parameters, crystal volume, and particle size of the samples are presented in Table 1. Interestingly, the trend of the lattice parameters and crystal volumes tended to be similar to the particle size pattern of the samples. For the maximum Mn ion composition, the lattice parameters and crystal volume increased significantly and decreased gradually with the increasing Zn ion composition. The crystal structure of the samples was similar to a previous study [22]. In this work, all samples had a spinel cubic structure [23], where the  $Mn^{2+}$ ,  $Zn^{2+}$ ,  $Fe^{2+}$ , and  $Fe^{3+}$  were randomly in octahedral and tetrahedral sites in the spinel system with lattice parameters of  $a = b = c$ .

With regard to the change in the crystal parameters with Zn and Mn doping, the cationic distribution of the spinel structure variate depends on the degree of inversion ( $i$ ). Based on the stoichiometry, the degree of inversion can be defined as the fraction of A-sites that are filled by cations and initially attributed to the B-sites. The  $Mn_{1-x}Zn_xFe_2O_4$  nanoparticles ( $0 < x < 1$ ) are defined by the cationic distribution shown in Eq. (1), according to the degree of inversion proposed by Klencsár et al. [24]. The

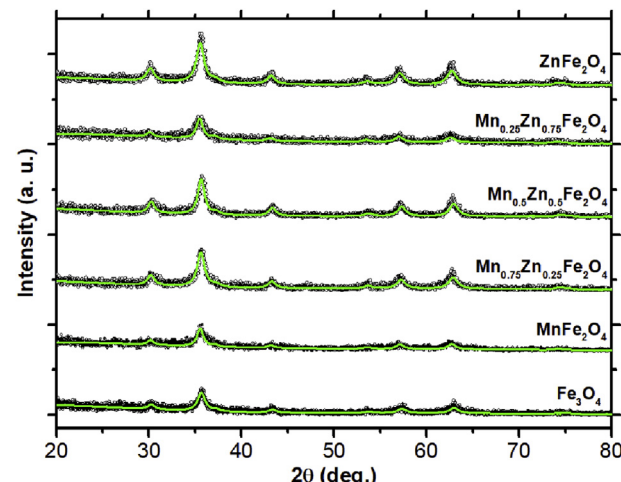


Figure 1. X-ray diffraction patterns of the  $Mn_{1-x}Zn_xFe_2O_4$  nanoparticles.

**Table 1.** Lattice parameters and particle size of the  $Mn_{1-x}Zn_xFe_2O_4$  nanoparticles.

Sample	Lattice parameters $a = b = c$ ( $\text{\AA}$ )	Crystal volume $V = a^3$ ( $\text{\AA}^3$ )	Particle size (nm)
$Fe_3O_4$	$8.351 \pm 0.005$	$582.4 \pm 0.6$	$9.5 \pm 0.3$
$MnFe_2O_4$	$8.380 \pm 0.003$	$588.5 \pm 0.6$	$11.5 \pm 0.3$
$Mn_{0.75}Zn_{0.25}Fe_2O_4$	$8.377 \pm 0.003$	$587.9 \pm 0.5$	$10.4 \pm 0.2$
$Mn_{0.5}Zn_{0.5}Fe_2O_4$	$8.372 \pm 0.002$	$586.8 \pm 0.7$	$9.8 \pm 0.2$
$Mn_{0.25}Zn_{0.75}Fe_2O_4$	$8.365 \pm 0.004$	$585.3 \pm 0.5$	$9.1 \pm 0.2$
$ZnFe_2O_4$	$8.349 \pm 0.003$	$581.9 \pm 0.7$	$10.1 \pm 0.3$

samples with  $x = 0.25, 0.50$ , and  $0.75$  have a degree of inversion of  $0.59, 0.50$ , and  $0.41$ , respectively. Furthermore, the degree of inversion of samples  $x = 0$  and  $1$  are  $0.37$  and  $0.68$ , respectively. Using the calculation model by Klencsár *et al.* [24] and Liu *et al.* [25], including applying the degree of inversion, the cationic distribution of samples  $x = 0$  and  $1$  can be expressed in Eqs. (2) and (3). Moreover, the cationic distribution of  $Fe_3O_4$  is presented in Eq. (4).

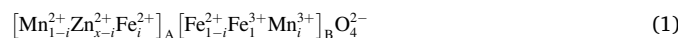
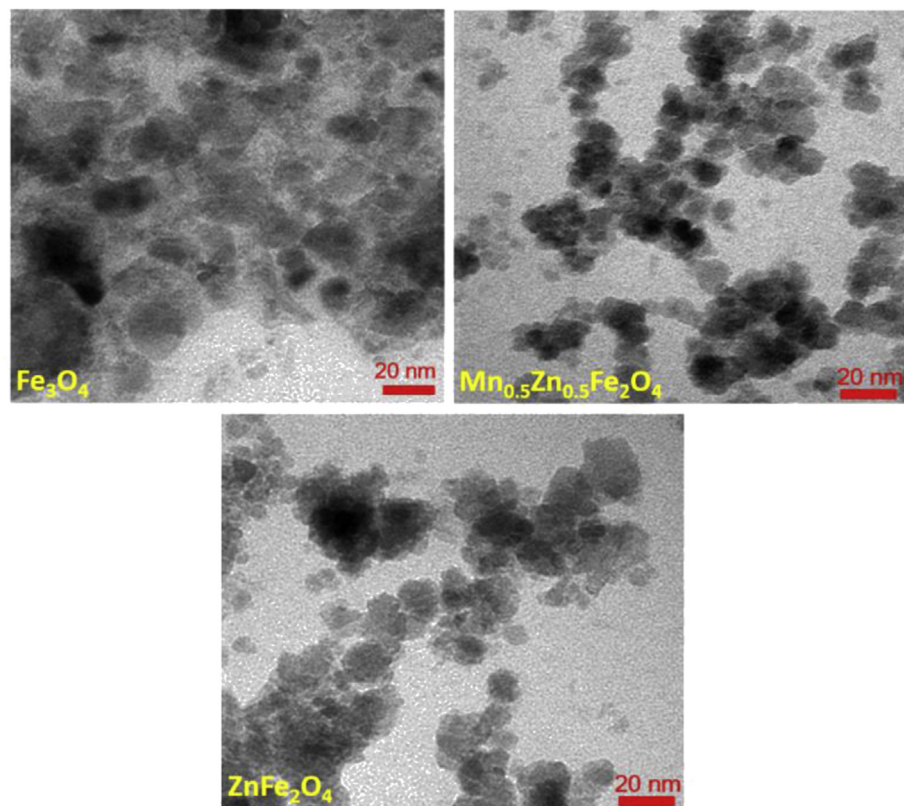


Figure 2 presents the TEM characterization illustrating the morphology of the  $Mn_{1-x}Zn_xFe_2O_4$  nanoparticles. The characterization focused on three samples,  $Fe_3O_4$ ,  $Mn_{0.5}Zn_{0.5}Fe_2O_4$ , and  $ZnFe_2O_4$  nanoparticles. As shown in Figure 2, the fabricated samples were nanometer in size. Based on a physics perspective, small magnetic nanoparticles have

high surface area, which leads to an increase in van der Waals force [26]. This force causes the  $Mn_{1-x}Zn_xFe_2O_4$  nanoparticles to agglomerate. The average particle size of the  $Fe_3O_4$ ,  $Mn_{0.5}Zn_{0.5}Fe_2O_4$ , and  $ZnFe_2O_4$  nanoparticles were  $11.1, 13.0$ , and  $10.3$  nm, respectively. Although the TEM characterization showed that the nanoparticles were successfully fabricated in a nanometer size, the particle size and hierarchical structure of the  $Mn_{1-x}Zn_xFe_2O_4$  ferrofluids could not be characterized. Therefore, an *in situ* investigation was conducted using a synchrotron-based SAXS to investigate the real particle size and hierarchical structure of the  $Mn_{1-x}Zn_xFe_2O_4$  ferrofluids. The SAXS profiles of the  $Mn_{1-x}Zn_xFe_2O_4$  ferrofluids and its fitting analysis are presented in Figure 3. The SAXS profiles were fitted using mathematical models as well as the form factor  $P(q,R)$ , structure factor  $S(q,R)$ , intensity  $I(q)$ , and distribution of particle size  $f(R)$ , as shown in Eqs. (5), (6), (7), and (8) [18, 27]:

$$P(q,R) = 9 \left[ \frac{\sin(qR) - qR \cos(qR)}{(qR)^3} \right]^2 \quad (5)$$

$$S(q,R) = 1 + \frac{D}{R_0^D} \int_0^\infty R^{D-3} h(R,\xi) \frac{\sin(qR)}{qR} R^2 dR \quad (6)$$

**Figure 2.** TEM images of the  $Mn_{1-x}Zn_xFe_2O_4$  nanoparticles.

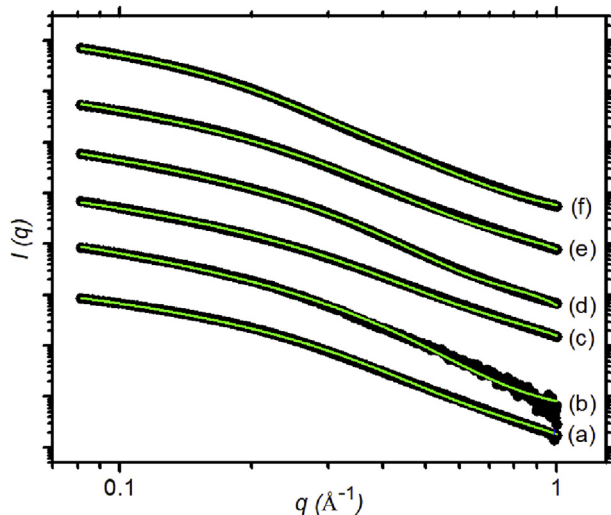


**Figure 3.** Synchrotron SAXS profiles of the (a)  $\text{Fe}_3\text{O}_4$ , (b)  $\text{MnFe}_2\text{O}_4$ , (c)  $\text{Mn}_{0.75}\text{Zn}_{0.25}\text{Fe}_2\text{O}_4$ , (d)  $\text{Mn}_{0.5}\text{Zn}_{0.5}\text{Fe}_2\text{O}_4$ , (e)  $\text{Mn}_{0.25}\text{Zn}_{0.75}\text{Fe}_2\text{O}_4$ , and (f)  $\text{ZnFe}_2\text{O}_4$  ferrofluids. The black circles and green solid lines represent the experimental data and fitting model, respectively.

$$I(q) = \int_0^\infty N_1(R_1)F_N^2(q, R_1)dR_1 + \int_0^\infty N_2(R_2)F_N^2(q, R_2)dR_2S(q, R_2, \xi, D) \quad (7)$$

$$f(R) = \frac{N}{\sigma R \sqrt{2\pi}} \exp\left[\frac{\ln^2(R/R_0)}{2\sigma^2}\right] \quad (8)$$

where  $q$  is the scattering vector,  $R$  is the particle size,  $\sigma$  is the polydispersity index,  $R_1$  is the primary particles,  $R_2$  is the secondary particles,  $R_0$  is the mean particle radii,  $N$  is the normalization factor,  $\xi$  is the cutoff length from fractal correlation, and  $D$  is the fractal dimension [20]. In general, the ferrofluids with a single surfactant stabilization have particle size distribution along with a polydisperse character and chain-like structure [28]. According to the theoretical approach, the particle size of the ferrofluids can be suitably fit with a lognormal model in constructing the fractal structures [29]. Specifically, the fitting analysis results of the SAXS data for the  $\text{Mn}_{1-x}\text{Zn}_x\text{Fe}_2\text{O}_4$  ferrofluids are presented in Table 2. The primary particles of the  $\text{Mn}_{1-x}\text{Zn}_x\text{Fe}_2\text{O}_4$  ferrofluids were spherical, with a diameter of 3.6–4.1 nm that formed secondary cluster particles, which is similar to the results of a previous work [30]. The primary particle building blocks constructed a fractal structure with a chain-like structure for all samples with a fractal dimension from 1.12 to 1.67. The primary particles built the secondary particles, constructing a fractal structure in one dimension as a chain-like-structure [31]. An illustration of the hierarchical structure of the  $\text{Mn}_x\text{Zn}_{1-x}\text{Fe}_2\text{O}_4$  ferrofluids is shown in Figure 4. Theoretically, the chain-like structure in the ferrofluids is built even in the presence of an external magnetic field.

The functional groups of the  $\text{Mn}_{1-x}\text{Zn}_x\text{Fe}_2\text{O}_4$  ferrofluids are presented in Figure 5. The stretching band of  $\text{Fe}^{3+}-\text{O}$  was observed at the

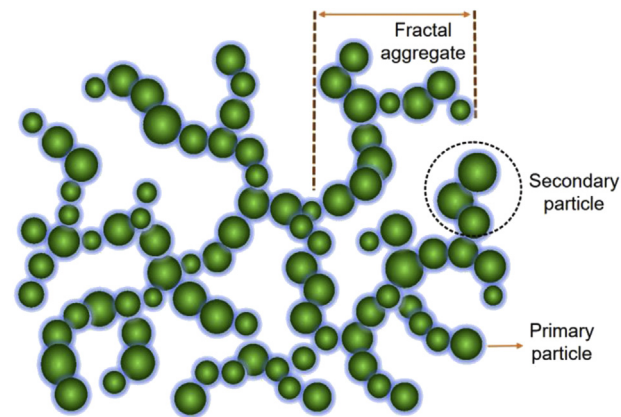


**Figure 4.** Illustration of the hierarchical structure of the  $\text{Mn}_{1-x}\text{Zn}_x\text{Fe}_2\text{O}_4$  ferrofluids.

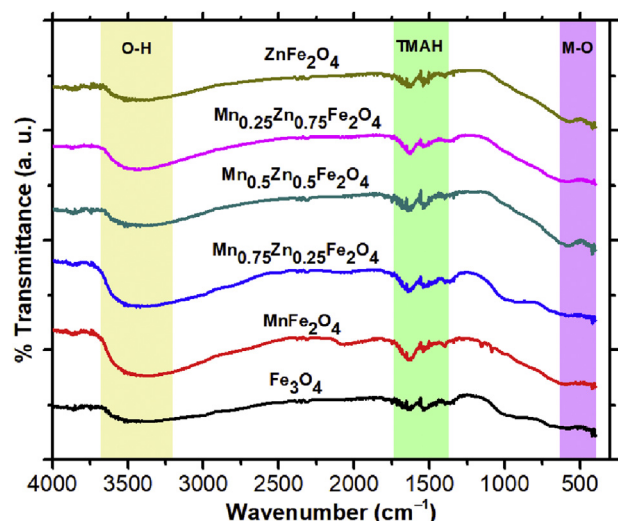


**Figure 5.** Infrared spectrum of the  $\text{Mn}_{1-x}\text{Zn}_x\text{Fe}_2\text{O}_4$  ferrofluids.

wavenumber of  $433\text{ cm}^{-1}$  and the band of  $\text{Fe}^{2+}-\text{O}$  was in the range of  $573$ – $634\text{ cm}^{-1}$  [32].  $\text{Fe}^{3+}-\text{O}$  and  $\text{Fe}^{2+}-\text{O}$  were located at the octahedral and tetrahedral sites. The functional groups of the metal–oxygen (M–O) group originated from the magnetic particles as fillers to form ferrofluids. The competition of the Mn and Zn ions at the octahedral and tetrahedral sites in the spinel system tended to change the lattice parameters of the  $\text{Mn}_{1-x}\text{Zn}_x\text{Fe}_2\text{O}_4$  ferrofluids. Furthermore, the presence of TMAH was evaluated by the functional group of the C–N, C–H, and O–H observed at the wavenumbers of  $1395$ ,  $1508$ , and  $3377\text{ cm}^{-1}$ , respectively [33]. The TMAH acted as a surfactant to cover the magnetic nanoparticles. Finally, the carrier liquid was detected by the functional group of O–H identified at the same position with the stretching band of the TMAH at the wavenumber of  $3379\text{ cm}^{-1}$  [34], broadening the peak for the O–H

**Table 2.** Results of the synchrotron SAXS fitting of the  $\text{Mn}_{1-x}\text{Zn}_x\text{Fe}_2\text{O}_4$  ferrofluids.

Sample	Primary particle (nm)	Secondary particle (nm)	Fractal aggregate (nm)	Fractal dimension
$\text{Fe}_3\text{O}_4$	$3.6 \pm 0.1$	$11.1 \pm 0.1$	$80.0 \pm 4.5$	$1.67 \pm 0.17$
$\text{MnFe}_2\text{O}_4$	$3.6 \pm 0.2$	$10.5 \pm 0.1$	$27.9 \pm 1.3$	$1.49 \pm 0.13$
$\text{Mn}_{0.75}\text{Zn}_{0.25}\text{Fe}_2\text{O}_4$	$4.1 \pm 0.2$	$13.9 \pm 0.2$	$68.7 \pm 3.6$	$1.36 \pm 0.11$
$\text{Mn}_{0.5}\text{Zn}_{0.5}\text{Fe}_2\text{O}_4$	$3.6 \pm 0.1$	$16.8 \pm 0.3$	$65.7 \pm 3.1$	$1.13 \pm 0.05$
$\text{Mn}_{0.25}\text{Zn}_{0.75}\text{Fe}_2\text{O}_4$	$4.0 \pm 0.2$	$13.0 \pm 0.2$	$32.8 \pm 1.0$	$1.40 \pm 0.10$
$\text{ZnFe}_2\text{O}_4$	$3.6 \pm 0.1$	$12.8 \pm 0.1$	$68.9 \pm 3.4$	$1.12 \pm 0.05$

stretching band. Therefore, all ferrofluid components were perfectly observed originating from the filler, surfactant, and carrier liquid.

The magnetic properties of the  $Mn_{1-x}Zn_xFe_2O_4$  ferrofluids were evaluated from the magnetization curves, as shown in Figure 6. The magnetization patterns of the ferrofluids tended to be different, specifically related to saturation magnetization. Theoretically, the smaller the particle size, the greater the magnetic moment on the surface. Under this condition, the magnetic moment on the surface contributes significantly to the magnetic properties of the materials. Kaur *et al.* explained that the saturation magnetization of magnetic nanoparticles in the spinel system depends on their magnetic moment and exchange interaction [22]. In the spinel structure, the magnetic moment is influenced by the atomic spin interaction mechanism at the A-site and B-site. Therefore, the net magnetic moment can be calculated using Eq. (9) [35].

$$\mu_{\text{net}} = \mu_{\text{B-site}} - \mu_{\text{A-site}} \quad (9)$$

By substituting the magnetic moment values of  $Fe^{2+}$  ( $4 \mu_B$ ),  $Mn^{2+}$  ( $5 \mu_B$ ),  $Zn^{2+}$  ( $0 \mu_B$ ),  $Fe^{3+}$  ( $5 \mu_B$ ), and  $Mn^{3+}$  ( $4 \mu_B$ ) into Eq. (9) and Eqs. (1), (2), (3), and (4), the net magnetic moment in the spinel system produced, as shown in Table 3. The calculated magnetic moment value has a different saturation magnetization pattern for each sample. Therefore, the magnetic properties of the ferrofluids are not only influenced by the net magnetic moment and exchange interaction, but also influenced by other factors, including particle dispersion, nanoparticle arrangement, and the energy of dipole interaction of two contacting particles [36]. Thus, the SAXS data provides an important role in explaining the correlation of the structure parameters of the ferrofluids to their magnetic properties.

In the ferrofluids, strong inter-particle interactions cause large magnetic particles to form chains. Under an external magnetic field, small magnetic particles can still maintain Brownian motion or link to the end of the chain. This behavior contributes to the change in the coercivity field and remanent magnetization of the ferrofluids. Based on Table 2, the  $ZnFe_2O_4$  ferrofluid sample has a large average aspect ratio (chain correlation length  $\xi = 68.9$  nm with secondary particles = 12.8 nm), which indicates that the sample has a large average anisotropy shape and implies an increase in the remanent magnetization. In this work,  $ZnFe_2O_4$  is ferrimagnetic because the magnetic moments located in the tetrahedral position are opposites within the octahedral position, resulting in unequal magnetic moments in the spinel system. The spinel system can be divided into three types: normal, inverse, and mixed spinel systems. In the previous work, Grasset *et al.* showed that the  $ZnFe_2O_4$  with a normal spinel exhibits antiferromagnetic character [37]. The diamagnetic  $Zn^{2+}$  ions are only at tetrahedral sites and  $Fe^{3+}$  ions are only at octahedral sites

and they are coupled with each other via a superexchange pathway through tetrahedral sites. Furthermore, other previous works showed that zinc ferrite nanoparticles are antiferromagnetic in a normal spinel system and with bulk materials; however, they show ferrimagnetic behavior at the nanometer scale. Other reports similarly showed that  $ZnFe_2O_4$  does not construct a normal spinel system.  $ZnFe_2O_4$  nanoparticles show ferrimagnetic behavior at room temperature and antiferromagnetic ordering below 9 K [38]. Other showed that the  $ZnFe_2O_4$  nanoparticles have ferrimagnetic behavior at room temperature [39, 40]. Interestingly, the  $ZnFe_2O_4$  ferrofluid sample has a fractal dimension of  $D \sim 1$ , which is interpreted as a chain arrangement resembling a rod. According to the theory, the demagnetization factor of the chain arrangement can be expressed by Eq. (10) [41].

$$D_{\text{factor}} = 1 - \left( \frac{\xi}{2r} \right) \left[ \left( 1 + \left( \frac{\xi}{2r} \right) \right)^2 \right]^{1/2} \quad (10)$$

The longer the chain arrangement, the smaller the  $D_{\text{factor}}$ . When the  $D_{\text{factor}}$  is low, the remanent magnetization increases. Furthermore, other ferrofluid samples have larger fractal dimension that interprets a denser chain arrangement with shorter chain lengths. Therefore, the coercivity field and remanent magnetization decrease.

Interestingly, the  $Mn_{0.5}Zn_{0.5}Fe_2O_4$  ferrofluids have a superparamagnetic character with the highest saturation magnetization value. However, compared to the bulk samples, the saturation magnetization of the ferrofluids was lower because of the effect of the surfactant and carrier liquid [42]. The surfactant and carrier liquid in the ferrofluids strongly contribute to creating repulsion forces between particles, thereby overcoming aggregation. If the particle interaction force is greater than the electrostatic repulsion force, the ferrofluids will be polydisperse; otherwise, the ferrofluids will be monodisperse. Based on the SAXS data analysis, the  $Mn_{1-x}Zn_xFe_2O_4$  ferrofluids belong to a bidisperse system because they contain two different particle sizes, namely primary and secondary particles. In the ferrofluid system, the small particles have Brownian motion, while the large particles have a stronger coupling interaction and dominate the Brownian motion [43]. Therefore, the saturation magnetization also depends on the behavior of the large particles. High saturation magnetization occurs with samples that have a large particle size and a polydisperse index, which is consistent with previous studies [42, 43, 44, 45].

The performance of the magnetic sensor was investigated by measuring the sensitivity of the  $Mn_{1-x}Zn_xFe_2O_4$  ferrofluids under an external magnetic field. The external magnetic field increased until the magnetic moment of the ferrofluids achieved saturation. Furthermore, the magnetic field was then reduced to obtain an output voltage as a function of the magnetic field, as shown in Figure 7. In general, when the ferrofluids was subject to an increasing external magnetic field, the output voltage also increased and vice versa. For the  $Fe_3O_4$  ferrofluids, the splitting curve was observed to start from the magnetic field of 10 mT. Therefore, the stability of the  $Fe_3O_4$  ferrofluids as magnetic sensors was not optimum. However, the  $MnFe_2O_4$  ferrofluids had high stability, which was identified from the relative absence of the splitting curve. This shows that  $MnFe_2O_4$  ferrofluids have high potential to be used as magnetic sensor materials for a small magnetic field. The results of this work coincide with the magnetic sensor developed by Zhao and co-workers based on ferrofluids combining with the photonic crystal fiber [46]. They observed that the ferrofluids characteristics change rapidly because of the magnetic field. The nearly coinciding curves of the increasing and decreasing magnetic field proves that the sensor performance is ideal. Furthermore, for  $Mn_{0.75}Zn_{0.25}Fe_2O_4$  ferrofluids, the magnetic sensor performance of the  $Mn_{0.75}Zn_{0.25}Fe_2O_4$  ferrofluids is not as good as the  $MnFe_2O_4$  ferrofluids for fields greater than 35 mT. This difference can be explained by the presence of Zn ions, which substitute the Mn ion to affect the magnetic moment of the sample. Moreover, the sensor performance curve of the  $Mn_{0.5}Zn_{0.5}Fe_2O_4$  ferrofluids fluctuates above the 35 mT because of the increased molar fraction of Zn ions. The  $Mn_{0.25}Zn_{0.75}Fe_2O_4$  and  $ZnFe_2O_4$  ferrofluids had a splitting curve,

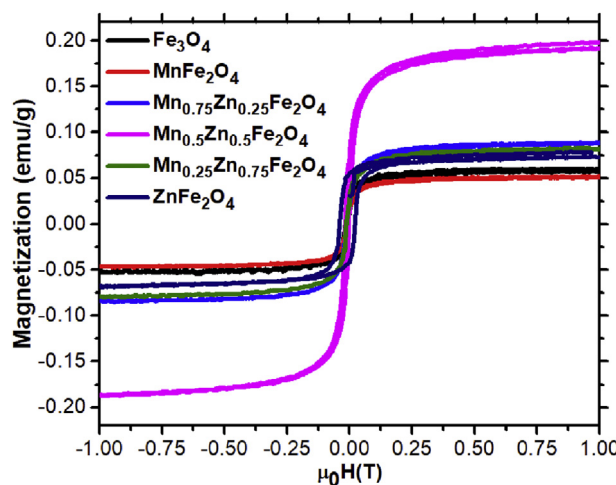


Figure 6. Magnetization curves of the  $Mn_{1-x}Zn_xFe_2O_4$  ferrofluids at room temperature.

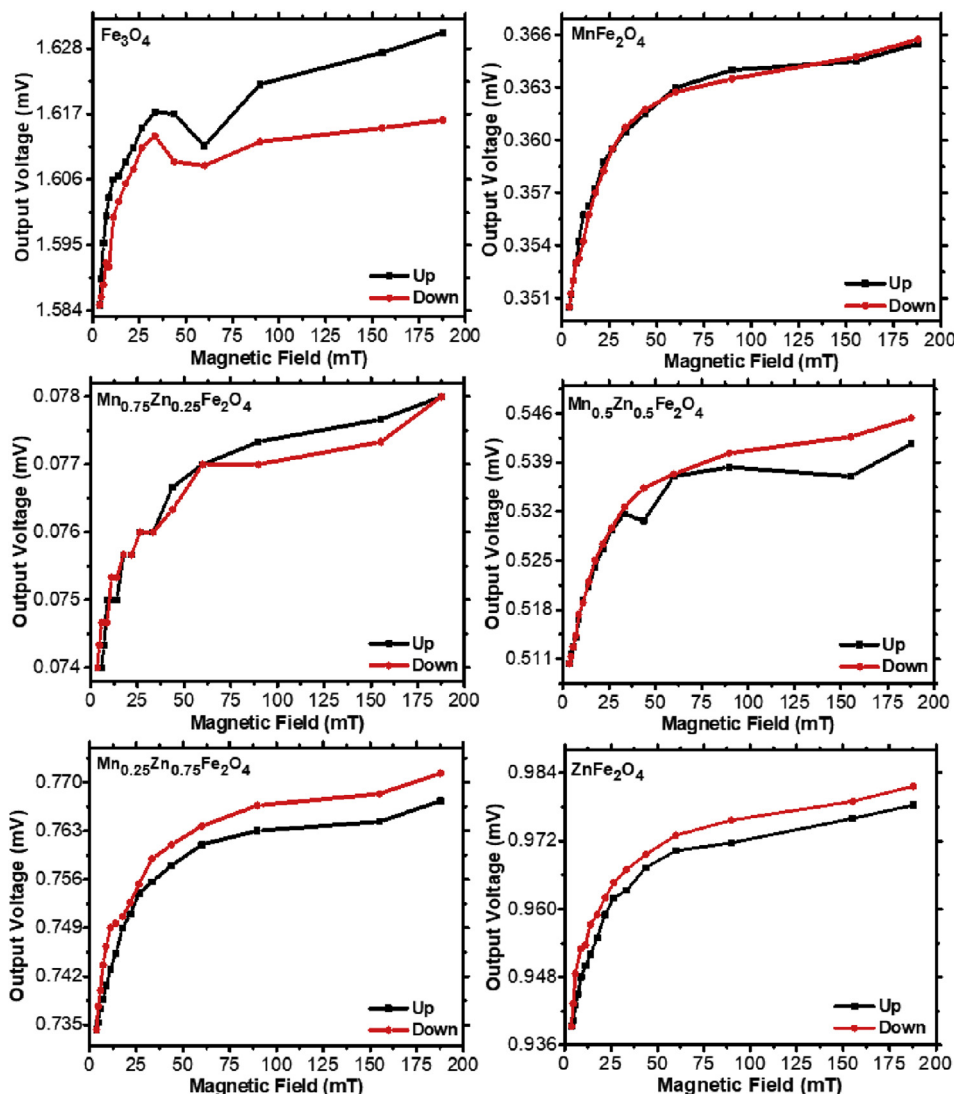
**Table 3.** Magnetic properties of the  $Mn_{1-x}Zn_xFe_2O_4$  ferrofluids.

Sample	Magnetic moment ( $\mu_B$ )	Saturation magnetization (emu/g)	Remanent magnetization (emu/g)	Secondary particle (nm)	Polydispersity index
$Fe_3O_4$	4.00	$0.053 \pm 0.004$	$3.4 \pm 0.2$	$11.1 \pm 0.1$	$0.13 \pm 0.03$
$MnFe_2O_4$	5.00	$0.046 \pm 0.004$	-	$10.5 \pm 0.1$	$0.11 \pm 0.02$
$Mn_{0.75}Zn_{0.25}Fe_2O_4$	4.59	$0.086 \pm 0.007$	$2.4 \pm 0.1$	$13.9 \pm 0.2$	$0.38 \pm 0.05$
$Mn_{0.5}Zn_{0.5}Fe_2O_4$	7.00	$0.188 \pm 0.008$	$4.2 \pm 0.2$	$16.8 \pm 0.3$	$0.41 \pm 0.04$
$Mn_{0.25}Zn_{0.75}Fe_2O_4$	4.41	$0.079 \pm 0.006$	$2.0 \pm 0.1$	$13.0 \pm 0.2$	$0.26 \pm 0.02$
$ZnFe_2O_4$	6.04	$0.070 \pm 0.005$	$4.1 \pm 0.2$	$12.8 \pm 0.1$	$0.29 \pm 0.05$

although with increasing Zn ion composition, the splitting becomes relatively narrow. Thus, the best magnetic sensor performance was observed with the  $MnFe_2O_4$  ferrofluids, which have excellent stability in both up and down fields.

The particle relaxation time is essential to ensure sensor performance. The output voltage as a function of the particle relaxation time of the  $Mn_{1-x}Zn_xFe_2O_4$  ferrofluids is shown in Figure 8. In a relatively short time, the magnetic particles in the ferrofluids were able to return to the initial state. This improves the sensor performance because the ferrofluids do not require a long time to relax, indicating that the ferrofluids as a magnetic sensor material have excellent flexibility. In general, the magnetic particles of the  $Mn_{1-x}Zn_xFe_2O_4$  ferrofluids, except  $Mn_{0.5}Zn_{0.5}Fe_2O_4$ ,

ferrofluids, tended to be easily and quickly stable after a mechanical treatment less than 3 min. We predict that this phenomenon is caused by secondary particles, where the  $Mn_{0.5}Zn_{0.5}Fe_2O_4$  ferrofluids are the largest. Because the secondary particles are large, the magnetic particles become easier and faster to precipitate. In this case, the particle relaxation time is defined as the time to of the magnetic particles of the ferrofluids to reach stability. The particle relaxation time is influenced by the particle motion characteristics of the ferrofluids. The closer the particles, the more limited the particle motion under mechanical treatment and it will quickly return to its original state after the treatment is removed [47]. This phenomenon is consistent with research conducted by Zhou and co-workers, demonstrating that ferrofluids have high

**Figure 7.** Magnetic sensor performance of the  $Mn_{1-x}Zn_xFe_2O_4$  ferrofluids at room temperature.

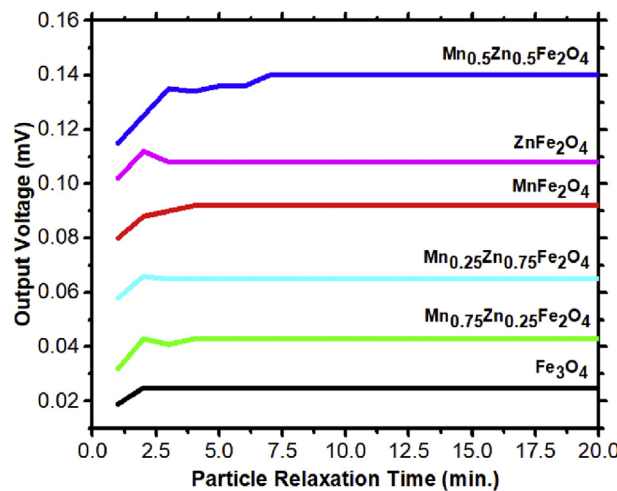


**Figure 8.** Particle relaxation time of the  $\text{Mn}_{1-x}\text{Zn}_x\text{Fe}_2\text{O}_4$  ferrofluids at room temperature.

flexibility [48]. Thus, if the ferrofluids are given an external treatment, then after the treatment is removed, it will quickly return to its original state.

The radar absorption performance of the  $\text{Mn}_{1-x}\text{Zn}_x\text{Fe}_2\text{O}_4$  nanoparticles was evaluated using a VNA at room temperature, and its result is presented in Figure 9. The experiment was conducted at a frequency range of 8–12 GHz for the working area of the radar. The reflection loss ( $RL$ ) as the ability of the samples to absorb the radar was evaluated using Eq. (11):

$$RL = 20 \log \left| \frac{1 - \sqrt{\mu_r/\epsilon_r} \tanh(-j2\pi f d \sqrt{\mu_r \epsilon_r})}{1 + \sqrt{\mu_r/\epsilon_r} \tanh(-j2\pi f d \sqrt{\mu_r \epsilon_r})} \right| \quad (11)$$

where  $\mu_r$  represents the complex permeability of the absorber,  $\epsilon_r$  represents the complex permittivity of the absorber,  $f$  represents the frequency,  $d$  represents the thickness of the absorber, and  $c$  represents the velocity of light in a vacuum [49]. In principle, good radar absorbing materials have special characteristics such as lightweight, thin, and the ability to cover a broad frequency [50].

Based on Figure 9, the  $RL$  of the samples was  $-14.1$ ,  $-15.4$ ,  $-12.9$ ,  $-11.0$ ,  $-12.9$ , and  $-11.7$  dB for the  $\text{Fe}_3\text{O}_4$ ,  $\text{MnFe}_2\text{O}_4$ ,  $\text{Mn}_{0.75}\text{Zn}_{0.25}\text{Fe}_2\text{O}_4$ ,  $\text{Mn}_{0.5}\text{Zn}_{0.5}\text{Fe}_2\text{O}_4$ ,  $\text{Mn}_{0.25}\text{Zn}_{0.75}\text{Fe}_2\text{O}_4$ , and  $\text{ZnFe}_2\text{O}_4$  samples, respectively. Such  $RL$  was observed at frequencies of  $10.8$ ,  $10.9$ ,  $10.8$ ,  $10.8$ ,  $10.9$ , and  $10.8$  GHz, respectively. The maximum peak was observed for the  $\text{MnFe}_2\text{O}_4$  sample, indicating that this sample exhibited the best performance as a radar absorbing material. Akinay and co-workers identified the radar absorbing performance of a polyvinyl butyral (PVB),  $\text{Fe}_3\text{O}_4$ , and nickel ferrite nanoparticle composite with various thicknesses [51]. The absorption peak was in the frequency range of  $1.0$ – $3.0$  GHz for the PVB/ $\text{Fe}_3\text{O}_4$  nanocomposites and  $1.0$ – $2.6$  GHz for the PVB/ $\text{NiFe}_2\text{O}_4$  nanocomposites with a minimum thickness of  $3$  mm. Theoretically, the absorbing phenomenon of the magnetic materials is initiated by the changing energy of the electromagnetic waves when the magnetic dipole moves to rotate in the material [52]. Based on the data analysis, increasing Zn or decreasing Mn in the  $\text{Mn}_{1-x}\text{Zn}_x\text{Fe}_2\text{O}_4$  nanoparticles decreases the  $RL$  because Zn is a diamagnetic material, reducing the energy needed to rotate the magnetic moment [53]. The  $\text{Mn}_{0.5}\text{Zn}_{0.5}\text{Fe}_2\text{O}_4$  nanoparticles had a minimum  $RL$  believed to be the effect of the largest secondary particle ( $16.8$  nm) with the highest polydispersity index ( $0.41$ ). With a larger particle size, the ratio of the surface area to volume is smaller, causing low absorption of the materials. Interestingly, the  $\text{MnFe}_2\text{O}_4$  nanoparticles with the highest Mn composition had a maximum  $RL$ . Based on the theoretical calculation,  $\text{Mn}^{2+}$  with a higher magnetic moment ( $5 \mu_B$ ) replaced  $\text{Fe}^{2+}$  with a lower magnetic moment ( $4 \mu_B$ ).

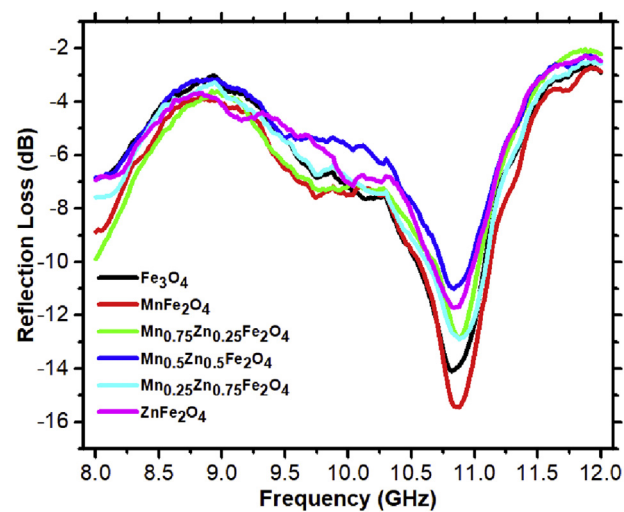


**Figure 9.** Reflection loss of the  $\text{Mn}_{1-x}\text{Zn}_x\text{Fe}_2\text{O}_4$  nanoparticles at a frequency range of 8–12 GHz.

$\mu_B$ ). Furthermore, the  $\text{MnFe}_2\text{O}_4$  nanoparticles with the smallest primary particles as building blocks contributed to the increasing surface area. Therefore, the  $\text{MnFe}_2\text{O}_4$  nanoparticles more easily absorbed the microwave. The microwave directed to the nanoparticles in the  $\text{Mn}_{1-x}\text{Zn}_x\text{Fe}_2\text{O}_4$  ferrofluids also interacts with the TMAH surfactant agent and carrier liquid that has dielectric characteristics. Therefore, a Coulomb force appears owing to the interaction between the electric field from the microwave and free radicals from the surfactant and dispersant [54]. Therefore, the microwave stimulates the charge acceleration that produces an electric current. In addition, the magnetic field of the ferrofluids generates destructive superposition with the opposite phase under the microwave [55]. Consequently, the radar that interacts with the  $\text{Mn}_{1-x}\text{Zn}_x\text{Fe}_2\text{O}_4$  ferrofluids was difficult to detect by the radar receiver. As a result, our  $\text{Mn}_{1-x}\text{Zn}_x\text{Fe}_2\text{O}_4$  ferrofluids are expected to form a novel platform for advancing radar absorbing materials.

#### 4. Conclusion

In this study, the synthesis of  $\text{Mn}_{1-x}\text{Zn}_x\text{Fe}_2\text{O}_4$  ferrofluids was performed through a coprecipitation method employing natural iron sand as the main precursor. As the Zn molar fraction increases, the lattice parameters, crystal volume, and particle size of the ferrofluids tended to decrease. In general, the  $\text{Mn}_{1-x}\text{Zn}_x\text{Fe}_2\text{O}_4$  nanoparticles had a spherical shape that were nanometer in scale. The functional groups for the main components of the  $\text{Mn}_{1-x}\text{Zn}_x\text{Fe}_2\text{O}_4$  ferrofluids were detected from the metal oxides, TMAH, and  $\text{H}_2\text{O}$  used as the filler, surfactant, and carrier liquid, respectively. The aggregation characteristics strongly contributed to the saturation magnetization of the  $\text{Mn}_{1-x}\text{Zn}_x\text{Fe}_2\text{O}_4$  ferrofluids. Furthermore, the potential of the ferrofluids as magnetic sensors was demonstrated by excellent performance, especially for the  $\text{MnFe}_2\text{O}_4$  ferrofluids. For radar absorbing applications, the maximum Mn composition presented the best performance because it was the smallest building block of the magnetic particles. Therefore, the ecofriendly  $\text{Mn}_{1-x}\text{Zn}_x\text{Fe}_2\text{O}_4$  nanoparticles fabricated from natural sand are potential magnetic sensors and radar absorbing materials.

#### Declarations

##### Author contribution statement

Ahmad Taufiq: Conceived and designed the experiments; Analyzed and interpreted the data; Wrote the paper.

Syamsul Bahtiar: Performed the experiments; Analyzed and interpreted the data.

Rosy Eko Saputro: Analyzed and interpreted the data; Wrote the paper.

Defi Yuliantika: Contributed reagents, materials, analysis tools or data.

Arif Hidayat: Analyzed and interpreted the data; Wrote the paper.

Sunaryono Sunaryono: Conceived and designed the experiments.

Nurul Hidayat: Analyzed and interpreted the data.

Samian Samian: Conceived and designed the experiments; Performed the experiments.

Siriwat Soontaranon: Analyzed and interpreted the data; Contributed reagents, materials, analysis tools or data.

#### Funding statement

This work was supported by Kementerian Riset Teknologi Dan Pendidikan Tinggi Republik Indonesia (071/SP2H/LT/DRPM/2018).

#### Competing interest statement

The authors declare no conflict of interest.

#### Additional information

No additional information is available for this paper.

#### References

- [1] P. Thakur, D. Chahar, S. Taneja, N. Bhalla, A. Thakur, A review on MnZn ferrites: synthesis, characterization and applications, *Ceram. Int.* 46 (2020) 15740–15763.
- [2] Ch. Srinivas, E.R. Kumar, P.N. Ramesh, M. Krishna, M.S. Singh, C.L. Prajapat, A. Verma, D.L. Sastry, Evaluation of structural and dielectric properties of Mn<sup>2+</sup>-substituted Zn-spinel ferrite nanoparticles for gas sensor applications, *Sensor. Actuator. B Chem.* 316 (2020) 128127.
- [3] B.H.K. Lopes, R.C. Portes, M.A. da Amaral Junior, D.E. Florez-Vergara, A.M. Gama, V.A. Silva, S.F. Quirino, M.R. Baldan, X Band electromagnetic property influence of multi-walled carbon nanotube in hybrid MnZn ferrite and carbonyl iron composites, *J. Mater. Res. Technol.* 9 (2020) 2369–2375.
- [4] T. Ma, Y. Cui, Y. Sha, L. Liu, J. Ge, F. Meng, F. Wang, Facile synthesis of hierarchically porous rGO/MnZn ferrite composites for enhanced microwave absorption performance, *Synth. Met.* 265 (2020) 116407.
- [5] E. Auzans, D. Zins, E. Blums, R. Massart, Synthesis and properties of Mn-Zn ferrite ferrofluids, *J. Mater. Sci.* 34 (1999) 1253–1260.
- [6] T. Haritha, K. Ramji, K.K. Murthy, P.S. Nagasree, D.B. Nagesh, Synthesis and Microwave Absorption Properties of MnZn Ferrite Nanocomposite, *Recent Trends in Mechanical Engineering*, Springer, Singapore, 2020, pp. 419–429.
- [7] A. Teber, K. Cil, T. Yilmaz, B. Eraslan, D. Uysal, G. Surucu, A.H. Baykal, R. Bansal, Manganese and zinc spinel ferrites blended with multi-walled carbon nanotubes as microwave absorbing materials, *Aerospace* 4 (2017) 2.
- [8] A. van Silfhout, B. Erné, Magnetic detection of nanoparticle sedimentation in magnetized ferrofluids, *J. Magn. Magn. Mater.* 472 (2019) 53–58.
- [9] Y. El Mendili, F. Grasset, N. Randrianantoandro, N. Neramour, J.-M. Grenache, J.-F. Bardeau, Improvement of thermal stability of maghemite nanoparticles coated with oleic acid and oleylamine molecules: investigations under laser irradiation, *J. Phys. Chem. C* 119 (2015) 10662–10668.
- [10] M. Latikka, M. Backholm, J.V.I. Timonen, R.H.A. Ras, Wetting of ferrofluids: phenomena and control, *Curr. Opin. Colloid Interface Sci.* 36 (2018) 118–129.
- [11] F. Spizzo, P. Sgarbossa, E. Sieni, A. Semenzato, F. Dugherio, M. Forzan, R. Bertani, L. Del Bianco, Synthesis of ferrofluids made of iron oxide nanoflowers: interplay between carrier fluid and magnetic properties, *Nanomaterials* 7 (2017) 373.
- [12] R.-Q. Lv, Y. Zhao, D. Wang, Q. Wang, Magnetic fluid-filled optical fiber Fabry-Pérot sensor for magnetic field measurement, *IEEE Photon. Technol. Lett.* 26 (2014) 217–219.
- [13] E. Shojaeizadeh, F. Veysi, K. Goudarzi, M. Feyzi, Magnetoviscous effect investigation of water based Mn-Zn Fe<sub>2</sub>O<sub>4</sub> magnetic nanofluid under the influence of magnetic field: an experimental study, *J. Magn. Magn. Mater.* 477 (2019) 292–306.
- [14] R. Arulmurugan, G. Vaidyanathan, S. Sendhilnathan, B. Jeyadevan, Mn-Zn ferrite nanoparticles for ferrofluid preparation: study on thermal-magnetic properties, *J. Magn. Magn. Mater.* 298 (2006) 83–94.
- [15] A. Taufiq, A. Niknah, A. Hidayat, S. Sunaryono, N. Mufti, N. Hidayat, H. Susanto, Synthesis of magnetite/silica nanocomposites from natural sand to create a drug delivery vehicle, *Heliyon* 6 (2020), e03784.
- [16] B. Hunter, Rietica - a visual Rietveld program, *IUCr Comm. Powder Diffraction Newslett.* 20 (1998) 21.
- [17] X. Lasheras, M. Insausti, J.M. de la Fuente, I. Gil de Muro, I. Castellanos-Rubio, L. Marcano, M.L. Fernández-Gubieda, A. Serrano, R. Martín-Rodríguez, E. Garaio, J.A. García, L. Lezama, Mn-doping level dependence on the magnetic response of Mn<sub>x</sub>Fe<sub>3-x</sub>O<sub>4</sub> ferrite nanoparticles, *Dalton Trans.* 48 (2019) 11480–11491.
- [18] A. Taufiq, Sunaryono, E.G. Rachman Putra, A. Okazawa, I. Watanabe, N. Kojima, S. Pratapa, Darminto, Nanoscale clustering and magnetic properties of Mn<sub>x</sub>Fe<sub>3-x</sub>O<sub>4</sub> particles prepared from natural magnetite, *J. Supercond. Nov. Magn.* 28 (2015) 2855–2863.
- [19] M. Li, Q. Gao, T. Wang, Y.-S. Gong, B. Han, K.-S. Xia, C.-G. Zhou, Solvothermal synthesis of Mn<sub>x</sub>Fe<sub>3-x</sub>O<sub>4</sub> nanoparticles with interesting physicochemical characteristics and good catalytic degradation activity, *Mater. Des.* 97 (2016) 341–348.
- [20] A. Taufiq, Sunaryono, N. Hidayat, A. Hidayat, E.G.R. Putra, A. Okazawa, I. Watanabe, N. Kojima, S. Pratapa, Darminto, Studies on nanostructure and magnetic behaviors of mn-doped black iron oxide magnetic fluids synthesized from iron sand, *Nano* 12 (2017) 1750110.
- [21] D.M. Bezerra, J.E.F.S. Rodrigues, E.M. Assaf, Structural, vibrational and morphological properties of layered double hydroxides containing Ni<sup>2+</sup>, Zn<sup>2+</sup>, Al<sup>3+</sup> and Zr<sup>4+</sup> cations, *Mater. Char.* 125 (2017) 29–36.
- [22] N. Kaur, B. Chudasama, Structure induced tunable magnetic properties of Zn substituted Mn<sub>1-x</sub>Zn<sub>x</sub>Fe<sub>2</sub>O<sub>4</sub> (x = 0–1) NPs, *Micro Nano Lett.* 12 (2017) 151–156.
- [23] S.M. Siddeeg, A. Amari, M.A. Tahoon, N.S. Alsaiari, F.B. Rebah, Removal of meloxicam, piroxicam and Cd<sup>2+</sup> by Fe<sub>3</sub>O<sub>4</sub>/SiO<sub>2</sub>/glycidyl methacrylate-S-SH nanocomposite loaded with laccase, *Alexandria Eng. J.* 59 (2020) 905–914.
- [24] Z. Klencsár, Gy. Tolnai, L. Korecz, I. Sajó, P. Németh, J. Osán, S. Mészáros, E. Kuzmann, Cation distribution and related properties of Mn<sub>x</sub>Zn<sub>1-x</sub>Fe<sub>2</sub>O<sub>4</sub> spinel nanoparticles, *Solid State Sci.* 24 (2013) 90–100.
- [25] J. Liu, Y. Bin, M. Matsuo, Magnetic behavior of Zn-doped Fe<sub>3</sub>O<sub>4</sub> nanoparticles estimated in terms of crystal domain size, *J. Phys. Chem. C* 116 (2012) 134–143.
- [26] P. Priyananda, H. Sabouri, N. Jain, B.S. Hawkett, Steric Stabilization of γ-Fe<sub>2</sub>O<sub>3</sub> superparamagnetic nanoparticles in a hydrophobic ionic liquid and the magnetorheological behavior of the ferrofluid, *Langmuir* 34 (2018) 3068–3075.
- [27] D. Yuliantika, A. Taufiq, E.G.R. Putra, Hierarchical structure and antibacterial activity of olive oil based MZF<sub>2</sub>O<sub>4</sub> ferrofluids, *J. Phys. Conf.* 1436 (2020), 012145.
- [28] A.A. Veligzhanin, D.I. Frey, A.V. Shulenina, A.Yu. Gruzinov, Ya.V. Zubavichus, M.V. Avdeev, Characterization of aggregate state of polydisperse ferrofluids: some aspects of anisotropy analysis of 2D SAXS in magnetic field, *J. Magn. Magn. Mater.* 459 (2018) 285–289.
- [29] A.Y. Cherny, E.M. Anitas, V.A. Osipov, A.I. Kuklin, Scattering from surface fractals in terms of composing mass fractals, *J. Appl. Crystallogr.* 50 (2017) 919–931.
- [30] F.L.D.O. Paula, SAXS Analysis of magnetic field influence on magnetic nanoparticle clusters, *Condens. Matter* 4 (2019) 55.
- [31] E. Woźniak, M. Štípková, M. Šlouf, V.M. Garamus, M. Šafaříková, I. Šafařík, M. Stepanek, Stabilization of aqueous dispersions of poly(methacrylic acid)-coated iron oxide nanoparticles by double hydrophilic block polyelectrolyte poly(ethylene oxide)-block-poly(N-methyl-2-vinylpyridinium iodide), *Colloids Surfaces A Physicochem. Eng. Aspects* 514 (2017) 32–37.
- [32] H.D. Nguyen, T.D. Nguyen, D.H. Nguyen, P.T. Nguyen, Magnetic properties of Cr doped Fe<sub>3</sub>O<sub>4</sub> porous nanoparticles prepared through a co-precipitation method using surfactant, *Adv. Nat. Sci. Nanosci. Nanotechnol.* 5 (2014), 035017.
- [33] F. Khan, S.-H. Baek, J.H. Kim, One-step and controllable bipolar doping of reduced graphene oxide using TMAH as reducing agent and doping source for field effect transistors, *Carbon* 100 (2016) 608–616.
- [34] A. Taufiq, F.N. Ikasari, D. Yuliantika, S. Sunaryono, N. Mufti, H. Susanto, E. Suarsini, N. Hidayat, A. Fuad, A. Hidayat, M. Diantoro, Structural, magnetic, optical and antibacterial properties of magnetite ferrofluids with PEG-20000 template, *Mater. Today Proc.* 17 (2019) 1728–1735.
- [35] W.D. Callister, D.G. Rethwisch, Materials Science and Engineering: an Introduction, eighth ed., John Wiley & Sons, Hoboken, NJ, 2010.
- [36] L. Gutiérrez, L. de la Cueva, M. Moros, E. Mazarío, S. de Bernardo, J.M. de la Fuente, M.P. Morales, G. Salas, Aggregation effects on the magnetic properties of iron oxide colloids, *Nanotechnology* 30 (2019) 112001.
- [37] F. Grasset, N. Labhsetwar, D. Li, D.C. Park, N. Saito, H. Haneda, O. Cador, T. Roismel, S. Mornet, E. Duguet, J. Portier, J. Etourneau, Synthesis and magnetic characterization of zinc ferrite nanoparticles with different environments: powder, colloidal solution, and zinc ferrite-silica core-shell nanoparticles, *Langmuir* 18 (2002) 8209–8216.
- [38] L. Andjelković, M. Šuljagić, M. Lakić, D. Jeremić, P. Vulić, A.S. Nikolić, A study of the structural and morphological properties of Ni-ferrite, Zn-ferrite and Ni-Zn-ferrites functionalized with starch, *Ceram. Int.* 44 (2018) 14163–14168.
- [39] S. Raveendran, M.M. Alam, Mohd.I.K. Khan, A. Dhayalan, S. Kannan, In situ formation, structural, mechanical and in vitro analysis of ZrO<sub>2</sub>/ZnFe<sub>2</sub>O<sub>4</sub> composite with assorted composition ratios, *Mater. Sci. Eng. C* 108 (2020) 110504.
- [40] K.L.S. Rodríguez, J.J.M. Quintero, H.H. Medina Chanduví, A.V.G. Rebaza, R. Faccio, W.A. Adeagbo, W. Hergert, C.E.R. Torres, L.A. Errico, Ab-initio approach to the stability and the structural, electronic and magnetic properties of the (001) ZnFe<sub>2</sub>O<sub>4</sub> surface terminations, *Appl. Surf. Sci.* 499 (2020) 143859.
- [41] J. Wang, S. Cao, S. Xia, N. Gan, The assembly of chain-like Ni arrays under magnetic field and its enhanced properties, *Int. J. Nanosci.* 9 (2010) 543–547.
- [42] A.O. Ivanov, S.S. Kantorovich, E.N. Reznikov, C. Holm, A.F. Pshenichnikov, A.V. Lebedev, A. Chremos, P.J. Camp, Magnetic properties of polydisperse ferrofluids: a critical comparison between experiment, theory, and computer simulation, *Phys. Rev. E* 75 (2007), 061405.
- [43] J.P. Huang, C. Holm, Magnetization of polydisperse colloidal ferrofluids: effect of magnetostriction, *Phys. Rev. E* 70 (2004), 061404.
- [44] V. Russier, C. de Montferrand, Y. Lalatonne, L. Motte, Size and polydispersity effect on the magnetization of densely packed magnetic nanoparticles, *J. Appl. Phys.* 112 (2012), 073926.
- [45] W. Xu-Fei, S. Li-Qun, Polydispersity effects on the magnetization of diluted ferrofluids: a lognormal analysis, *Chinese Phys. B* 19 (2010) 107502.

- [46] Y. Zhao, D. Wu, R.-Q. Lv, Magnetic field sensor based on photonic crystal fiber taper coated with ferrofluid, *IEEE Photon. Technol. Lett.* 27 (2015) 26–29.
- [47] J. Sólyom, *Fundamentals of the Physics of Solids: Structure and Dynamics*, Springer, Berlin ; New York, 2007.
- [48] Y. Zhou, L. Song, L. Yu, X. Xuan, Inertially focused diamagnetic particle separation in ferrofluids, *Microfluid. Nanofluidics* 21 (2017) 1–14.
- [49] G. Shen, M. Xu, Z. Xu, Double-layer microwave absorber based on ferrite and short carbon fiber composites, *Mater. Chem. Phys.* 105 (2007) 268–272.
- [50] A. Munir, Microwave radar absorbing properties of multiwalled carbon nanotubes polymer composites: a review, *Adv. Polym. Technol.* 36 (2017) 362–370.
- [51] Y. Akinay, F. Hayat, M. Çakir, E. Akin, Magnetic and microwave absorption properties of PVB/Fe<sub>3</sub>O<sub>4</sub> and PVB/NiFe<sub>2</sub>O<sub>4</sub> composites, *Polym. Compos.* 39 (2018) 3418–3423.
- [52] K. Praveena, K. Sadhana, S. Mattepanavar, H.-L. Liu, Effect of sintering temperature on the structural, dielectric and magnetic properties of Ni<sub>0.4</sub>Zn<sub>0.2</sub>Mn<sub>0.4</sub>Fe<sub>2</sub>O<sub>4</sub> potential for radar absorbing, *J. Magn. Magn Mater.* 423 (2017) 343–352.
- [53] P. Smitha, I. Singh, M. Najim, R. Panwar, D. Singh, V. Agarwala, G. Das Varma, Development of thin broad band radar absorbing materials using nanostructured spinel ferrites, *J. Mater. Sci. Mater. Electron.* 27 (2016) 7731–7737.
- [54] Y. Zare, M.H. Shams, M. Jazirehpour, Tuning microwave permittivity coefficients for enhancing electromagnetic wave absorption properties of FeCo alloy particles by means of sodium stearate surfactant, *J. Alloys Compd.* 717 (2017) 294–302.
- [55] W. Li, C. Li, L. Lin, Y. Wang, J. Zhang, All-dielectric radar absorbing array metamaterial based on silicon carbide/carbon foam material, *J. Alloys Compd.* 781 (2019) 883–891.